

## OBSERVATIONAL SIGNATURES OF THE CORONAL KINK INSTABILITY WITH THERMAL CONDUCTION

G. J. J. BOTHA<sup>1</sup>, T. D. ARBER<sup>1</sup>, AND ABHISHEK K. SRIVASTAVA<sup>2</sup>

<sup>1</sup> Physics Department, Centre for Fusion, Space and Astrophysics, University of Warwick, Coventry CV4 7AL, UK; G.J.J.Botha@warwick.ac.uk, T.D.Arber@warwick.ac.uk

<sup>2</sup> Aryabhatta Research Institute of Observational Sciences (ARIES), Nainital 263129, India; aks@aries.res.in

Received 2011 August 8; accepted 2011 October 12; published 2011 December 29

### ABSTRACT

It is known from numerical simulations that thermal conduction along magnetic field lines plays an important role in the evolution of the kink instability in coronal loops. This study presents the observational signatures of the kink instability in long coronal loops when parallel thermal conduction is included. The three-dimensional nonlinear magnetohydrodynamic equations are solved numerically to simulate the evolution of a coronal loop that is initially in an unstable equilibrium. The loop has length 80 Mm, width 8 Mm, and an initial maximum twist of  $\Phi = 11.5\pi$ , where  $\Phi$  is a function of the radius. The initial loop parameters are obtained from a highly twisted loop observed in the *Transition Region and Coronal Explorer (TRACE)* 171 Å wave band. Synthetic observables are generated from the data. These observables include spatial and temporal averaging to account for the resolution and exposure times of *TRACE* images. Parallel thermal conduction reduces the maximum local temperature by up to an order of magnitude. This means that different spectral lines are formed and different internal loop structures are visible with or without the inclusion of thermal conduction. However, the response functions sample a broad range of temperatures. The result is that the inclusion of parallel thermal conductivity does not have as large an impact on observational signatures as the order of magnitude reduction in the maximum temperature would suggest; the net effect is a blurring of internal features of the loop structure.

**Key words:** instabilities – magnetic fields – magnetohydrodynamics (MHD) – Sun: corona

**Online-only material:** color figures

### 1. INTRODUCTION

The magnetohydrodynamic (MHD) kink instability in cylindrical geometry serves as a first approximation for this instability in coronal loops. Its evolution has been studied numerically for more than a decade (Mikić et al. 1990; Baty & Heyvaerts 1996; Lionello et al. 1998; Arber et al. 1999). Previous work studied the onset of the kink instability by rotating a flux tube's footpoints until the twist increased beyond the critical value (Galsgaard & Nordlund 1997; Gerrard et al. 2002). Curvature effects have also been incorporated into the model by studying a kink-unstable flux tube, curved in a half-torus with its footpoints anchored in the same plane (Török et al. 2004; Török & Kliem 2005; Gerrard et al. 2004).

In another series of studies, the ideal MHD kink instability has been evoked as a trigger for reconnection occurring in coronal loops (Browning & Van der Linden 2003; Browning et al. 2008; Hood et al. 2009; Bareford et al. 2010). A cylinder is initialized with a twisted magnetic field profile that is unstable, and is then perturbed to evolve into the kink instability. Botha et al. (2011) have shown that by including thermal conduction along magnetic field lines in these models, the maximum temperature obtained during reconnection events is lowered by an order of magnitude, activating different spectral lines than when no parallel thermal conduction is included.

In this paper, the observational signatures of the MHD kink instability, with thermal conduction included, are presented and compared with a simulation without thermal conduction. A kink-unstable cylinder is evolved and the numerical results are compared to observations of a twisted coronal loop (Srivastava et al. 2010). In order to facilitate the comparison between the observed and forward modeled loops, the initial conditions are

obtained from the observations of Srivastava et al. (2010). The numerical results are filtered through the *Transition Region and Coronal Explorer (TRACE)* temperature response function in the 171 Å band before synthetic images of spatially and temporally averaged line-of-sight intensity measurements are presented, as in Haynes & Arber (2007).

The paper is divided into two main parts. In the first part the model is described, which includes a short description of the physical model, the initial conditions of the numerical simulation, and how the synthetic images were obtained from the numerical data. In the second part, the numerical results are discussed and the synthetic intensity images are generated from the data.

### 2. MODEL

The coronal loop is initialized as a straight twisted cylinder in a uniform background temperature and density.

#### 2.1. Physical Model

Nonlinear three-dimensional simulations are performed using the MHD Lagrangian-remap code, Lare3d, as described by Arber et al. (2001). It solves the resistive MHD equations for a fully ionized plasma, with a heat flux included in the energy equation. A full description of the physical model is given in Botha et al. (2011).

Thermal conduction is included along the magnetic field in the form of the classical Spitzer–Härm (1953), or Braginskii, conductivity with  $\log \Lambda = 18.4$ . This corresponds to the standard thermal conductivity parallel to the magnetic field of  $\kappa_{\parallel} = 10^{-11} T^{5/2} \text{ W m}^{-1} \text{ K}^{-1}$  (Priest 2000). Radiative losses do not play an important role and are not included in the model.

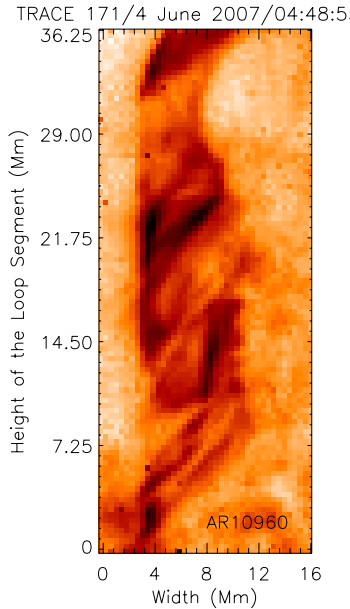


**Figure 1.** Observed loop system used as a source for the initialization of the simulations. Half of the loop length is shown with the helicity of the right-handed twist clearly visible. A time evolution of the complete loop system is presented by Figure 5 in Srivastava et al. (2010). The image is in reverse color. (A color version of this figure is available in the online journal.)

For the coronal values used in the model, the radiative cooling time is of order hours. During the simulations reconnection and heating occur within short lengths along the loop, typically one-tenth of the loop length (Botha et al. 2011). When the conductive cooling time is calculated for this length, it is in the order of minutes.

The code contains an artificial resistivity that is activated only when and where the current exceeds a critical value. It is of the form

$$\eta = \begin{cases} \eta_0, & |j| \geq j_c, \\ 0, & |j| < j_c, \end{cases} \quad (1)$$

where  $\eta_0$  is the anomalous resistivity and  $j_c = 2$  mA is the critical current.  $\eta_0$  is activated as soon as the kink instability occurs and then it stays active for the duration of the simulation (Botha et al. 2011).

## 2.2. Initialization Data

The data used to obtain the initial conditions of the simulated coronal loop are obtained from observations of a highly twisted loop (Srivastava et al. 2010). The loop was situated in AR NOAA 10960 and was observed on 2007 June 4 between 04:43 UT and 04:52 UT. *Solar and Heliospheric Observatory (SOHO)/Michelson Doppler Imager (MDI)*, *Hinode/Solar Optical Telescope (SOT) G band (4504 Å)*, and *Hinode/SOT Ca II H (3968 Å)* were used, respectively, to observe the photospheric and chromospheric parts of the active region and the associated highly twisted loop, while *TRACE 171 Å* was used to observe its coronal part. Figure 1 shows a close-up of approximately half of the observed loop system in *TRACE 171 Å*, 6 minutes after the activation of helical twist in the loop during the flaring process.

From the observations it is estimated that the loop length is  $\sim 80$  Mm and its radius in the corona is  $\sim 4$  Mm. This aspect ratio of 1:10 is within the observed range for coronal

loops (Klimchuk 2000; Watko & Klimchuk 2000; Aschwanden & Boerner 2011). The width of 8 Mm is larger than the usually observed coronal loop width of 2–4 Mm. Given that active region coronal loops change between 40% and 70% in diameter between their base in the upper transition region or lower corona and their apex (Brooks et al. 2007), we assume that the loop radius at its footpoints in the upper transition region is 2 Mm. One of the footpoints of the active region loop was above a positive polarity sunspot (Srivastava et al. 2010) and it is estimated that the lower bound of the magnetic field strength at this location was approximately 470 G. The minimum average strength of the magnetic field is estimated by assuming the homogeneous distribution of measured magnetic fluxes above the selected region over the positive polarity sunspot. However, the strength of the magnetic field may change at various locations above it between its minimum and maximum values. From this photospheric value the chromospheric magnetic field strength is calculated. Petrie & Patrikeeva (2009) found that the photospheric field is mostly vertical while the chromospheric field has no preferred direction. Since we are considering a magnetic loop, the assumption is made that most of the photospheric magnetic field goes to the chromosphere. However, this would be an upper limit. Kozlova & Somov (2009) looked at 36 sunspots and found that from a height of 100–1850 km the magnetic field strength diminishes between 0.1 and 0.7 G km<sup>-1</sup>, with the mean field gradient  $0.35 \pm 0.05$  G km<sup>-1</sup>. Using a magnetic field gradient of 0.2 G km<sup>-1</sup> and the field strength at the photosphere, the magnetic field strength at a height of 1850 km is calculated to be 80 G. If we assume that the field strength changes little between the upper chromosphere and the upper transition region, then the flux through the loop footpoint (radius 2 Mm) is  $10^{19}$  Mx. With the assumption of flux conservation along the loop, the magnetic field strength at the loop apex (radius 4 Mm) is 20 G. This led us to initialize the loop with a maximum field strength of 20 G inside the loop, while the background outside the loop contains a uniform field of 15 G that is parallel to the cylindrical axis.

In the numerical simulations the coronal loop is initialized as a uniform cylinder in force-free equilibrium and unstable to an ideal MHD kink instability (Hood et al. 2009). The axial twist is given by

$$\Phi = \frac{LB_\theta}{rB_z} \quad \text{with} \quad \max(\Phi) = 11.5\pi, \quad (2)$$

where  $L$  is the loop length and  $r$  is its radius. The axial magnetic field is given by  $B_z$  and the azimuthal field by  $B_\theta$ . Both  $B_\theta$  and  $B_z$  are functions of  $r$ . The maximum twist is at position  $r = 1$  Mm, with zero twist on the loop axis and at its edge. The radial profile of the twist is presented in Figure 2(b) in Hood et al. (2009). The maximum number of twists (six full turns) is chosen from the observational analysis of the highly twisted loop system shown in Figure 1, where three full turns are clearly visible. The total of six turns is estimated by extrapolating to the invisible part of the loop by assuming a symmetric loop shape.  $\max(\Phi)$  exceeds the stability threshold so that the loop is kink unstable. The critical value for a twist in a cylinder was found numerically to be  $4.8\pi$  (Mikić et al. 1990), while linear theory predicts it to be  $2.5\pi$  (Gerrard et al. 2002). Galsgaard & Nordlund (1997) found that the critical twist angle is a function of the loop diameter, field strength, and magnetic resistivity in the model. A full description of the magnetic field structure used in the simulations is given in Botha et al. (2011).

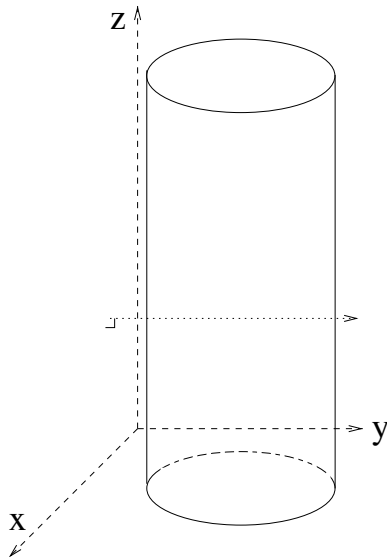


**Figure 2.** Schematic showing the orientation of the cylindrical loop in the Cartesian numerical domain. The dotted line indicates the integration path of the line-of-sight integral (Equation (3)) along the  $y$ -direction and perpendicular to the  $(x, z)$  plane.

Gravity is absent in the simulations. The initial temperature and mass density are chosen to be uniform and constant. The mass density has a value of  $1.67 \times 10^{-12} \text{ kg m}^{-3}$  (Young et al. 2009) and the temperature 0.125 MK. This temperature was chosen to make the evolution of the kink instability visible for the *TRACE* satellite. During the evolution of the kink instability the temperature increases locally where reconnection occurs (Botha et al. 2011). Through trial and error the initial temperature was chosen so that these high temperatures will be visible using the *TRACE* 171 Å temperature response function.

The evolution of the coronal loop is studied in Cartesian geometry (Figure 2). The boundaries in the  $(x, y)$  plane perpendicular to the loop axis are at  $\pm 8 \text{ Mm}$  and reflective. Thus, the loop's edge and the outer boundaries are 4 Mm apart. This distance proved to be adequate so that no feedback from the boundaries influences the numerical results. Along the loop axis the boundaries are at  $\pm 40 \text{ Mm}$  with velocities held at zero and the temperature fixed at the initial background value but allowing temperature gradients. Hence, a heat flux across the ends of the loop exists. The grid resolution in  $(x, y, z)$  is given by  $128 \times 128 \times 256$ .

### 2.3. Image Generation

The images generated from the numerical simulations were obtained by using the temperature response functions of *TRACE* (Schrijver et al. 1999) as well as those of *Solar Dynamics Observatory (SDO)/Atmospheric Imaging Assembly (AIA)*; Aschwanden & Boerner 2011). Details of the line contributions for the *TRACE* channels are in Handy et al. (1999) and for the *SDO/AIA* channels are in O'Dwyer et al. (2010). The emission is calculated at every node of the numerical grid and then integrated along the  $y$ -direction perpendicular to the axis of the loop, as indicated in Figure 2. The line-of-sight integral is given by

$$I = \int_{-L_y}^{+L_y} g(T) \rho^2 dy, \quad (3)$$

where  $I$  is the measured intensity,  $g(T)$  is the temperature response function of the respective instruments, and  $\rho$  is

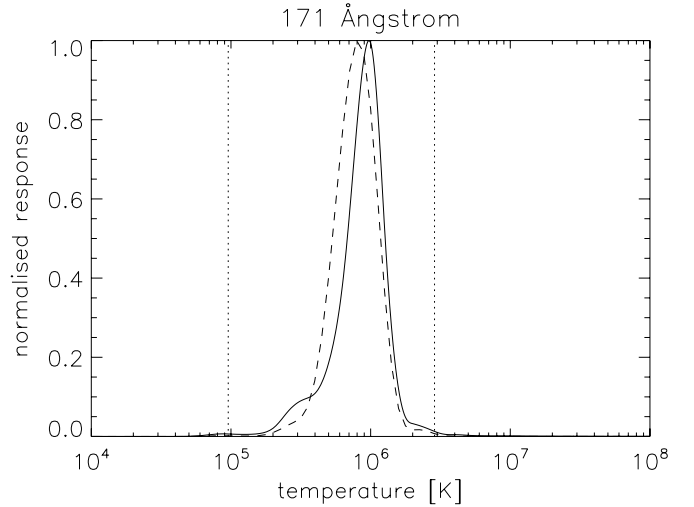


**Figure 3.** Normalized temperature response functions for *TRACE* 171 Å (solid line) and *SDO/AIA* 171 Å (broken line). The two vertical dotted lines are, respectively, the minimum and maximum temperatures during the simulation with parallel thermal conduction included, as measured in Figures 5 and 6.

the mass density. Figure 3 presents the temperature response functions of *TRACE* and *SDO/AIA* for 171 Å. This integration produces intensity images in the  $(x, z)$  plane, which are then integrated over time, with the time interval determined by the exposure time of the instrument. For *TRACE* this is taken to be 31.9 s and for *SDO/AIA* the time interval is 2.9 s. Finally, the time-integrated image is degraded by spatially averaging over squares of  $0.375 \times 0.375 \text{ Mm}^2$  to compensate for the pixel resolution of both *TRACE* and *SDO/AIA*. The process is illustrated in Figure 4 using the *TRACE* 171 Å temperature response function as given in Figure 3.

## 3. DISCUSSION

Two simulated data sets are presented: with and without thermal conduction parallel to the magnetic field lines. All other parameters and initial conditions are kept identical between the two runs. The physical consequences due to the inclusion of parallel thermal conduction are discussed by Botha et al. (2011). In this paper, the line-of-sight intensity contours are presented as observed through *TRACE* response functions. As such, only physical processes that are needed to explain the observables are included. The density and temperature from both data sets are used with *TRACE* response functions to generate intensity contours that can be compared with observational data.

After initialization, the kink-unstable loop evolves through a linear phase that lasts for 300 s, as is evident from Figure 5. During the nonlinear phase the kink instability drives magnetic field into a current sheet, where reconnection occurs and the temperature reaches a maximum due to the energy released. Subsequently, thermal conduction along magnetic field lines transports heat along the magnetic field lines away from the points where the plasma was heated by reconnection. The timescale for the evolution of the kink instability is the same with and without thermal conduction (Figures 5 and 6). In the case without thermal conduction, the heat due to reconnection is not conducted along magnetic field lines and the temperature maximum is higher. This can be seen in Figure 5 where the maximum temperature reached without parallel thermal conduction is 9 MK, compared to a maximum of 3 MK with thermal conduction. The physical processes during the kink instability, with

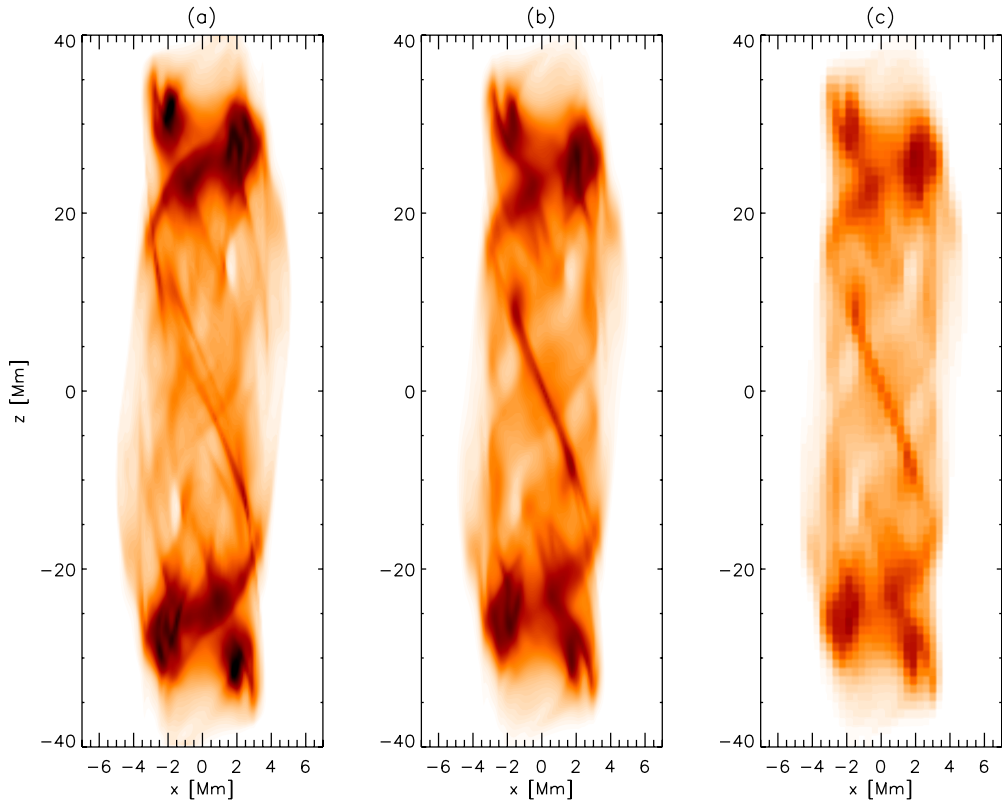


**Figure 4.** Intensity from the line-of-sight integration (Equation (3)) using the simulation data as filtered through the *TRACE* 171 Å temperature response function in Figure 3: (a) the simulation data at 417.6 s, (b) the time-averaged data set, and (c) the time and spatially averaged data set. The time exposure is 31.9 s and the spatial resolution is 0.375 Mm pixel<sup>-1</sup>. The images are in reverse color, with white representing the lowest value on the scale. The minimum and the maximum values of the reverse color scale are the same as those used in Figure 7. These data sets were taken from the simulation with parallel thermal conduction.

(A color version of this figure is available in the online journal.)

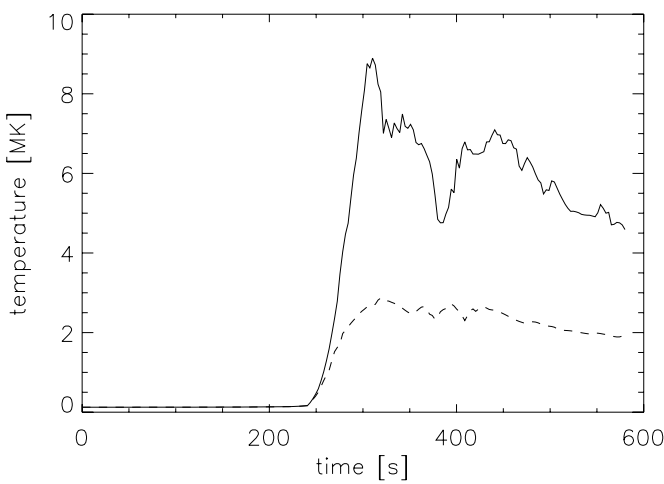


**Figure 5.** Maximum temperatures during the evolution of the kink instability for the two numerical runs with thermal conductivity included (broken line) and without thermal conduction (solid line).

and without thermal conduction, are discussed in more detail by Botha et al. (2011).

The emission, as observed in the *TRACE* 171 Å band, is presented in Figures 7 and 8 for the cases with and without parallel thermal conduction. Figure 3 shows that the temperature response function lies within the range determined by the minimum and maximum temperatures from the simulation with thermal conduction (Figures 5 and 6). The higher maximum temperature obtained without thermal conduction (Figure 5) causes the temperature response function to sample different

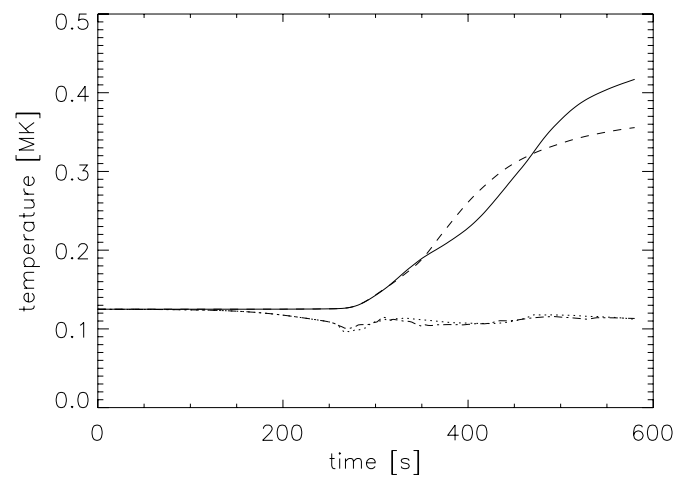


**Figure 6.** Temperatures during the evolution of the kink instability for the two numerical runs with and without thermal conductivity. The mean temperature is represented by a solid line for the simulation without thermal conduction and a broken line with thermal conductivity, similar to Figure 5. The mean temperature is calculated by averaging over the entire data cube. The minimum temperatures are also included, with the dash-dot-dashed line the simulation without thermal conduction and the dotted line with thermal conductivity.

aspects of the evolution of the kink instability. However, Figure 6 shows that the average loop temperatures with and without thermal conduction are comparable, making the intensity images in Figures 7 and 8 not radically different. This is due to the fact that heating occurs only at small localized areas, from where heat is then conducted along magnetic field lines. Figures 7

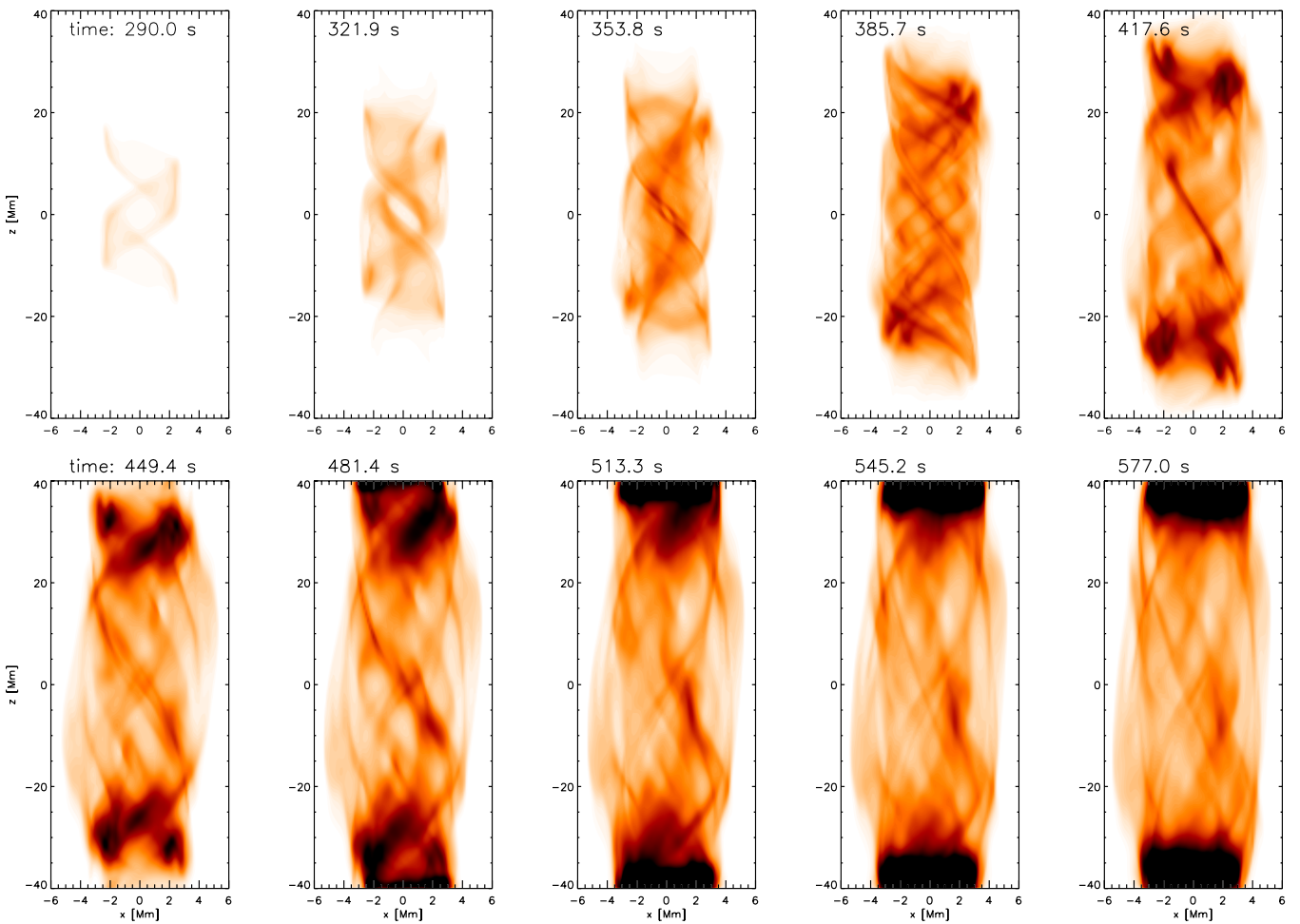


**Figure 7.** Simulated intensities as would be seen through the TRACE 171 Å filter of the kink and its aftermath, with thermal conduction included in the calculation. The first image is taken at 290.0 s and the cadence is 31.9 s. The time exposure, spatial resolution, and light intensity scale are the same as in Figure 4. The reverse color table is such that the minimum intensity (white) is chosen so that the lowest 10% of the simulation values at time 290 s are eliminated from these plots. All the exposures use the same reverse color scale.

(A color version of this figure is available in the online journal.)

and 8 show that the kink instability causes the same structures to form in both cases. Thermal conductivity causes the temperature to spread along magnetic field lines, resulting in images the features of which are less defined when compared with the images generated from data without thermal conductivity.

Irrespective of the inclusion or exclusion of thermal conductivity, the emission images show that the footpoints of the loops increase their emission during the nonlinear phase of the kink instability. The line-of-sight integral (Equation (3)) is determined by the temperature response function as well as the mass density. Figure 9 gives the temperature and mass density profiles along the central axis toward the end of the simulation for the case when thermal conduction is included. Note that the central axis experiences some heating (it has higher temperatures than the average temperatures in Figure 6) but the locations with maximum temperature are not on it (as it has lower temperatures than the maxima in Figure 5). Figure 9 shows that the enhanced emission is due to a density increase at the footpoints—and not footpoint heating. Plasma flows from the middle of the numerical domain, where current sheets form and reconnection occurs, driven by MHD ponderomotive forces generated during the kink instability. Footpoint brightening due to compression was also observed in the coronal loop simulations of Haynes & Arber (2007).

One factor that determines the onset of the nonlinear phase of the kink instability is the initial twist (Equation (2)) in the coronal loop. A smaller value of  $\max(\Phi)$  increases the duration of the linear phase. However, it was found that once the nonlinear phase is reached, the formation of the current sheet, the reconnection and the thermal aftermath have the same duration as long as the initial twist exceeds the stability threshold.

The first image in Figure 7 is sampled at 290.0 s and shows the twisted structure toward the end of the linear phase of the kink instability. In the second image (at 321.9 s) the nonlinear phase has formed a current sheet and in the third image (at 353.8 s) thermal conduction has transported heat from the reconnection site along the magnetic field lines. From 321.9 s the evolution of the internal loop structure along its length is observed for 4 minutes until the end of the numerical run at 577.0 s. As reconnection occurs within the loop, magnetic field lines straighten out along the length of the loop (Haynes & Arber 2007). At the same time heat is transported along magnetic field lines away from reconnection sites, so that the loop cools and its internal structure becomes less defined (Botha et al. 2011).

The differences in intensity images with and without thermal conduction are clear when the intensity images at 449.5 s and later times in Figures 7 and 8 are compared. Despite the

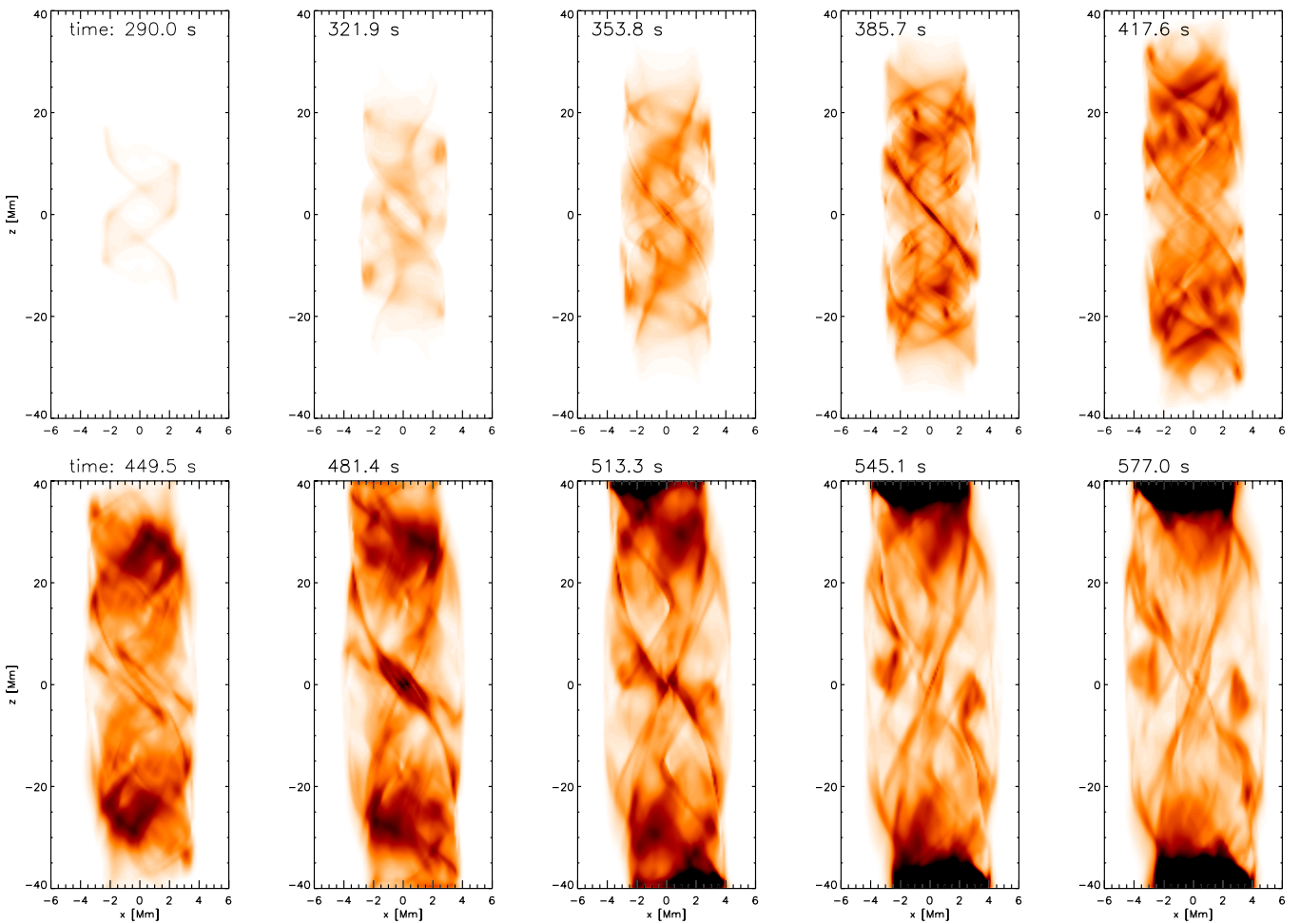


**Figure 8.** Simulated intensities as would be seen through the *TRACE* 171 Å filter of the kink and its aftermath, without thermal conduction. The exposure time, spatial resolution, and light intensity scale are the same as in Figure 4, with the minimum intensity (white) and the maximum (black) of the reverse color table having the same values as in Figure 7. The images are taken at the same times as those in Figure 7.

(A color version of this figure is available in the online journal.)

order of magnitude reduction in the maximum temperature when thermal conduction is included (Figure 5), similar looking internal loop structures are visible in the intensity images with and without thermal conduction. The response functions capture a range of temperatures (Figure 3) and because the average temperatures in the coronal loops are of similar values (Figure 6), the observational signatures are less sensitive to the inclusion of parallel thermal conduction. The main effect due to the inclusion of thermal conduction is the blurring of the internal features of the coronal loop, which is due to the efficient conduction of heat along magnetic field lines. In the simulation with thermal conduction the maximum temperature of the magnetic structures is closer to the average loop temperature (Figure 6) than the maximum temperature obtained without thermal conduction. Consequently, the internal loop structure is not as clearly delineated in the emission intensity as when no thermal conduction is present, which can be seen when comparing Figures 7 and 8.

In Figures 7 and 8, it appears that the amount of twist toward the end of the linear phase (at 290 s) is approximately three turns—instead of the six turns dictated by  $\max(\Phi)$  in Equation (2). The heating caused by the kink instability is highly localized and only magnetic field lines that pass through the heated area are visible. The physical processes associated

with this are discussed by Botha et al. (2011). As the twist is a function of the radius, one should not expect the line-of-sight integral (Equation (3)) to capture the heating that occurs at  $\max(\Phi)$ .

When comparing the numerical results with observations, it is more realistic to compare the results obtained when thermal conduction is included in the model. Figure 1 shows a loop segment of the observations from Srivastava et al. (2010) at a time in its evolution when the twisted threads are most visible in the observed images. The simulation images in Figure 7 show a similar fine internal structure, but it is clear that a perfect visual or quantitative match is not possible. As an example of this, Figure 7 at time 353.8 s or 385.7 s shows the twist to be one full turn over 40 Mm, while the observed image shows a full turn to be over 20 Mm.

In this paper, the results were obtained from only one initial equilibrium state. It is possible that other initial conditions may lead to end results that correspond closer with the observations of Srivastava et al. (2010). This needs further investigation. We also ignored curvature and gravity, both of which may be important during the evolution of the kink instability. Assuming the shape of the loop to be a perfect half-circle, the top of the loop will be 25 Mm above the transition region. The average and maximum temperatures inside the loop during

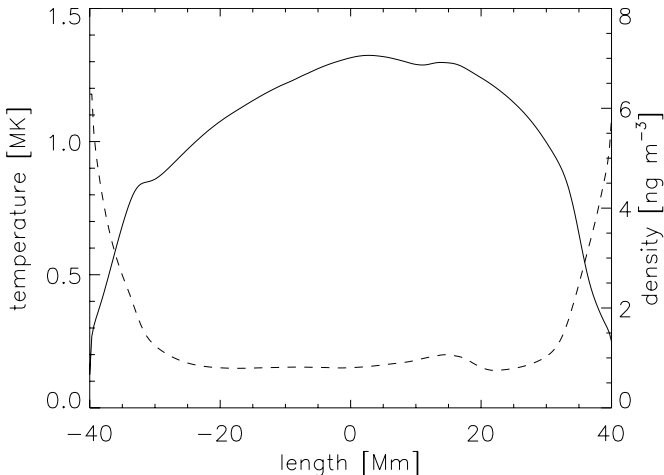


**Figure 9.** Temperature and mass density profiles along the length of the loop on its central axis at time 579.98 s, obtained from the simulation with thermal conduction. The solid line is the temperature and the dashed line is the mass density. Initialization is with a constant temperature of 0.125 MK and a constant density of  $1.67 \text{ ng m}^{-3}$ .

evolution of the kink instability are approximately 0.3 MK and 2 MK, respectively. These temperatures give gravitational scale heights of approximately 20 Mm and 120 Mm. Thus, density stratification is important and gravity cannot be ignored in the forward modeling of the kink instability for this loop. The inclusion of both curvature and gravity should be investigated further.

The observations of Srivastava et al. (2010) show that after the heating event, the loop structure cools down within 5 minutes to photospheric temperatures. The duration of the simulations presented here shows 4.5 minutes of the nonlinear evolution of the kink instability. During this time the average temperature of the loop increases (Figure 6) while the maximum temperature (with thermal conduction included) stays approximately the same (Figure 5). The reason for this is that as the current sheets evolve, multiple reconnection acts as a continuous heating source of the plasma inside the loop, with the location of the heating changing as the current sheets change (Hood et al. 2009).

The temperature response function for the *SDO/AIA* 171 Å band is presented in Figure 3. The emissions in 171 Å for *SDO/AIA* and *TRACE* are essentially the same because their temperature response functions lie so close together. The only difference between the two observational platforms is the time resolution. With the *TRACE* exposure time 11 times longer than that of *SDO/AIA*, the images from *SDO/AIA* are sharper.

In addition to the figures presented in this paper, the response functions from *TRACE* 195 Å and 284 Å as well as those for the coronal bandwidths of *SDO/AIA* were used in calculating the line-of-sight integral (Equation (3)). In all cases a broad range of temperatures are sampled from the simulated data, with a large part of the temperature range common to all the response functions. As a result, the differences between the line intensity plots were minor; the same basic internal loop structure was observed with no new information to be gained from them.

#### 4. CONCLUSION

The evolution of a coronal loop is studied, solving the resistive MHD equations for a fully ionized plasma and with parallel thermal conduction included in the model. The loop is initialized as a straight cylinder with a twist above the stability threshold, which leads to the kink instability. Line-of-sight

emission intensities of the simulation data were calculated using the temperature response functions from *TRACE*.

The simulations were initialized with physical parameters extracted from the observations of a coronal loop shown in Figure 1 (Srivastava et al. 2010). Figure 5 in Srivastava et al. (2010) shows the time evolution of a helically twisted structure of a flaring loop in *TRACE* 171 Å that is observed for 4 minutes. The initial magnetic field structure used in the simulations is a kink-unstable force-free equilibrium where the twist varies with radius (Hood et al. 2009). This field structure was used in previous studies of the kink instability (see Botha et al. 2011, and references therein) and although its maximum twist is similar to the global estimated twist from the observations of Srivastava et al. (2010), there is no guarantee that it is similar to the magnetic field of the observed loop. Throughout the evolution of the kink instability, the internal structure of the simulated loop is shown in the generated images (Figure 7). This structure evolves into a simpler configuration as the kink instability causes multiple reconnection events, which have the effect of straightening the internal magnetic field. In contrast, the observations of Srivastava et al. (2010) show a field structure that stays largely intact for the duration of the observations.

Footpoint brightening due to compression of the plasma is observed in the simulation results, but is absent from the observations of Srivastava et al. (2010). In the simulation this is due to the impenetrable boundaries of the numerical domain, which cause the plasma density to increase at the top and bottom boundaries of the loop axis (Figure 9). On the Sun, plasma moves through the transition region to the chromosphere and photosphere. It may be that footpoint brightening occurs in these lower regions, but the plasma is so cool that most likely it will not be captured by the response functions for coronal temperatures in spite of collective footpoint heating, although Srivastava et al. (2010) have observed bright points at coronal temperatures that may be evidence of localized footpoint heating.

Thermal conduction in the model conducts heat along magnetic field lines. The kink instability heats up the plasma where the current sheet causes reconnection. With thermal conduction included, this heat is transported along the magnetic field lines away from the reconnection sites. As a result, simulations without thermal conduction reach maximum temperatures of up to an order of magnitude larger than when thermal conduction is present (Figure 5 and Botha et al. 2011). In contrast, when the line-of-sight integral (Equation (3)) is calculated, the response functions of *TRACE* capture a broad range of temperatures. The average temperatures with and without thermal conduction are similar (Figure 6) and as a result the observational difference due to the inclusion of thermal conduction is much less, as can be seen when comparing Figures 7 and 8.

This paper considers the observational effects of including parallel thermal conduction into the model. Moving toward more realistic coronal loop simulations, a temperature profile and gravity need to be included, the latter of which adds density stratification to the system. Curvature is another part that is missing from the present study, which should be included at a later stage.

A.K.S. thanks Shobhna Srivastava for patient encouragements.

#### REFERENCES

- Arber, T. D., Longbottom, A. W., Gerrard, C. L., & Milne, A. M. 2001, *J. Comput. Phys.*, 171, 151

- Arber, T. D., Longbottom, A. W., & Van der Linden, R. A. M. 1999, *ApJ*, **517**, 990  
 Aschwanden, M. J., & Boerner, P. 2011, *ApJ*, **732**, 81  
 Bareford, M. R., Browning, P. K., & Van der Linden, R. A. M. 2010, *A&A*, **521**, A70  
 Baty, H., & Heyvaerts, J. 1996, *A&A*, **308**, 935  
 Botha, G. J. J., Arber, T. D., & Hood, A. W. 2011, *A&A*, **525**, A96  
 Brooks, D. H., Warren, H. P., Ugarte-Urra, I., Matsuzaki, K., & Williams, D. R. 2007, *PASJ*, **59**, S691  
 Browning, P. K., Gerrard, C., Hood, A. W., Kevis, R., & Van der Linden, R. A. M. 2008, *A&A*, **485**, 837  
 Browning, P. K., & Van der Linden, R. A. M. 2003, *A&A*, **400**, 355  
 Galsgaard, K., & Nordlund, Å. 1997, *J. Geophys. Res.*, **102**, 219  
 Gerrard, C. L., Arber, T. D., & Hood, A. W. 2002, *A&A*, **387**, 687  
 Gerrard, C. L., Hood, A. W., & Brown, D. S. 2004, *Sol. Phys.*, **222**, 79  
 Handy, B. N., Acton, L. W., Kankelborg, C. C., et al. 1999, *Sol. Phys.*, **187**, 229  
 Haynes, M., & Arber, T. D. 2007, *A&A*, **467**, 327  
 Hood, A. W., Browning, P. K., & Van der Linden, R. A. M. 2009, *A&A*, **506**, 913  
 Klimchuk, J. A. 2000, *Sol. Phys.*, **193**, 53  
 Kozlova, L. M., & Somov, B. V. 2009, *Mosc. Univ. Phys. Bull.*, **64**, 541  
 Lionello, R., Schnack, D. D., Einaudi, G., & Velli, M. 1998, *Phys. Plasmas*, **5**, 3722  
 Mikić, Z., Schnack, D. D., & Van Hoven, G. 1990, *ApJ*, **361**, 690  
 O'Dwyer, B., Del Zanna, G., Mason, H. E., Weber, M. A. D., & Tripathi, D. 2010, *A&A*, **521**, A21  
 Petrie, G. J. D., & Patrikeeva, I. 2009, *ApJ*, **699**, 871  
 Priest, E. R. 2000, Solar Magnetohydrodynamics (Geophysics and Astrophysics Monographs, Vol. 21; Dordrecht: Reidel), Section 2.3.2  
 Schrijver, C. J., Title, A. M., Berger, T. E., et al. 1999, *Sol. Phys.*, **187**, 261  
 Spitzer, L., & Härm, R. 1953, *Phys. Rev.*, **89**, 977  
 Srivastava, A. K., Zaqrashvili, T. V., Kumar, P., & Khodachenko, M. L. 2010, *ApJ*, **715**, 292  
 Török, T., & Kliem, B. 2005, *ApJ*, **630**, L97  
 Török, T., Kliem, B., & Titov, V. S. 2004, *A&A*, **413**, L27  
 Watko, J. A., & Klimchuk, J. A. 2000, *Sol. Phys.*, **193**, 77  
 Young, P. R., Watanabe, T., Hara, H., & Mariska, J. T. 2009, *A&A*, **495**, 587